Article

Ultrafast deposition of faceted lithium polyhedra by outpacing SEI formation

https://doi.org/10.1038/s41586-023-06235-w

Received: 2 December 2022

Accepted: 17 May 2023

Published online: 2 August 2023

Check for updates

Xintong Yuan[1], Bo Liu[1], Matthew Mecklenburg[2] & Yuzhang Li[1]✉

Electrodeposition of lithium (Li) metal is critical for high-energy batteries[1]. However, the simultaneous formation of a surface corrosion film termed the solid electrolyte interphase (SEI)[2] complicates the deposition process, which underpins our poor understanding of Li metal electrodeposition. Here we decouple these two intertwined processes by outpacing SEI formation at ultrafast deposition current densities[3] while also avoiding mass transport limitations. By using cryogenic electron microscopy[4–7], we discover the intrinsic deposition morphology of metallic Li to be that of a rhombic dodecahedron, which is surprisingly independent of electrolyte chemistry or current collector substrate. In a coin cell architecture, these rhombic dodecahedra exhibit near point-contact connectivity with the current collector, which can accelerate inactive Li formation[8]. We propose a pulse-current protocol that overcomes this failure mode by leveraging Li rhombic dodecahedra as nucleation seeds, enabling the subsequent growth of dense Li that improves battery performance compared with a baseline. While Li deposition and SEI formation have always been tightly linked in past studies, our experimental approach enables new opportunities to fundamentally understand these processes decoupled from each other and bring about new insights to engineer better batteries.

Uncontrolled lithium (Li) dendritic deposition morphologies pose poor cycling efficiency, short lifetime and significant safety concerns[9–11]. The simultaneously formed solid electrolyte interphase (SEI) layer controls lithium ion (Li^+) transport to the depositing surface[12], which in turn, influences the deposition morphology, generating a complex feedback loop of SEI formation and Li deposition that is difficult to decouple. This concurrent Li deposition and SEI growth underpin our incomplete understanding of how to precisely control Li morphology. For example, four common morphologies of Li metal (for example, filaments[5,13], nanorods[14–16], columns[17,18] or chunks[19,20]) formed in the model electrolytes shown in Fig. 1a all exhibit distinct Coulombic efficiencies (CEs), yet it remains unclear how various electrolyte chemistries lead to certain Li deposition morphologies. While a number of past studies[21] have attempted to rationalize Li deposition morphologies in different electrolytes, a general framework for understanding and predicting Li deposition morphology remains elusive due to the coupled growth of SEI and Li. A paradigm shift in understanding Li electrodeposition requires these two processes to be decoupled. However, SEI formation occurs simultaneously with Li electrodeposition because metallic Li is extremely reactive[22], immediately reacting with the liquid electrolyte to form the SEI[23]. In principle, Li electrodeposition and SEI formation can be decoupled if Li^+ can be reduced at faster timescales than electrolyte decomposition. Since electrolyte decomposition occurs on the order of seconds, high current densities are needed to outpace SEI influence during Li metal electrodeposition.

Here, we decouple Li deposition from SEI growth using an ultramicroelectrode (UME) geometry[3,24–26] (Supplementary Fig. 1) and surprisingly, observe that the diverse Li morphologies in the model electrolytes all transition to a well-defined faceted polyhedron at ultrafast current densities (Fig. 1a). This result seems counterintuitive, as previous studies showed that Li dendrites grow increasingly ramified at higher current density[13,27], yet it aligns with expectations if Li deposition truly proceeds independently from SEI formation. Cryogenic electron microscopy (cryo-EM) quantitatively identifies this morphology to be that of a rhombic dodecahedron, which matches the theoretical Wulff structure prediction of a body-centred cubic (bcc) crystal in the absence of a surface film. Furthermore, we discover that this well-defined faceted morphology persists independent of electrolyte chemistry or current collector substrate, which indicates that outpacing SEI influence can eliminate the effect of these parameters on Li deposition morphology. While these Li rhombic dodecahedra are poorly connected to the current collector and may accelerate inactive Li formation, we overcome this failure mode by proposing a pulse-current strategy that leverages these Li polyhedra as nucleation seeds for enabling improved reversibility of Li plating and stripping.

At high current densities, it is well known[13] that Li metal transitions from base-growing filaments to tip-growing dendritic Li upon diffusion-limited ion depletion at the electrolyte–Li interface. To avoid encountering mass transport limitations at high deposition rates, we used a UME as the depositing substrate. With a limiting current density that scales inversely with the radius, the 25-μm-diameter UME allows three-dimensional diffusion pathways toward the working electrode to sustain ultrafast current densities without sudden ion depletion. COMSOL Multiphysics simulations confirm that at 1,000 mA cm^{-2},

[1]Department of Chemical and Biomolecular Engineering, University of California, Los Angeles, Los Angeles, CA, USA. [2]California NanoSystems Institute, University of California, Los Angeles, Los Angeles, CA, USA. ✉e-mail: yuzhangli@ucla.edu

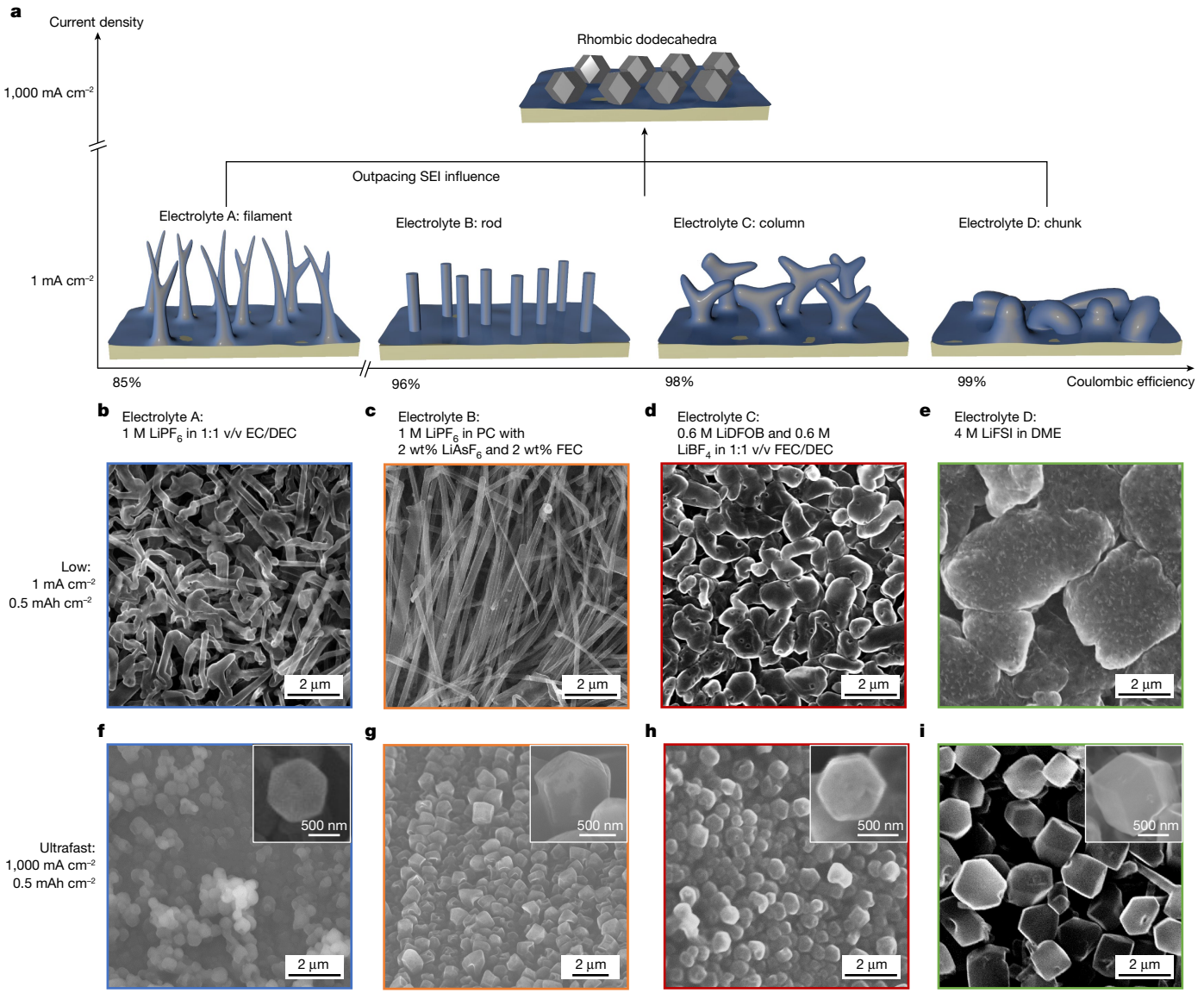

Fig. 1 | Transition of different dendritic Li to identical faceted Li polyhedra. **a**, Schematic of the distinct Li electrodeposition morphology as a function of electrolyte chemistry and current density. **b**–**e**, Li deposition in the Li||Cu coin cell at 1 mA cm^{-2} as filaments in electrolyte A (**b**), rods in electrolyte B (**c**), columns in electrolyte C (**d**) and chunks in electrolyte D (**e**). **f**–**i**, Faceted Li polyhedra deposited on UME at 1,000 mA cm^{-2} in electrolyte A (**f**), electrolyte B (**g**), electrolyte C (**h**) and electrolyte D (**i**). The insets are magnified images of individual faceted particles.

no significant depletion of Li^+ occurred on the working electrode surface (Supplementary Fig. 2)[28,29]. To deposit metallic Li at both normal and ultrafast rates, we chose four model electrolytes for their diversity in chemistry (for example, carbonate versus ether solvent, low versus high salt concentration, single versus dual salts and with versus without additives), which results in widely varying SEI layers, Li deposition morphologies and CE[4,17,19,30]: electrolyte A, 1 M lithium hexafluorophosphate ($LiPF_6$) in 1:1 v/v ethylene carbonate (EC)/diethyl carbonate (DEC); electrolyte B, 1 M $LiPF_6$ in propylene carbonate (PC) with 2 wt% lithium hexafluoroarsenate ($LiAsF_6$) and 2 wt% fluoroethylene carbonate (FEC); electrolyte C, 0.6 M lithium difluoro(oxalato)borate (LiDFOB) and 0.6 M lithium tetrafluoroborate ($LiBF_4$) in 1:1 v/v FEC/DEC; electrolyte D, 4 M lithium bis(fluorosulfonyl)imide (LiFSI) in dimethoxyethane (DME). While these electrolytes form distinct SEI layers that govern battery performance[31,32] under normal operating conditions (1–10 mA cm^{-2}), we expect the SEI and electrolyte chemistry to have diminished influence at ultrafast deposition regimes (50–1,000 mA cm^{-2}) that are predicted to outpace SEI growth.

Upon Li deposition at typical current densities, we found distinct Li morphologies in each of the model electrolytes (for example, 'filaments' in electrolyte A, 'rods' in electrolyte B, 'columns' in electrolyte C and 'chunks' in electrolyte D), as shown in Fig. 1b–e. While these qualitative descriptions highlight our incomplete understanding of Li deposition morphology, they are commonly used to explain key differences in macroscale battery performance between these electrolytes. For example, electrolytes C and D exhibit much higher CE (approximately 97–99%) than electrolyte A (approximately 85%) due to the lower surface area to volume ratio of the Li deposits. Interestingly, at an ultrafast current density of 1,000 mA cm^{-2}, we discover a stark morphological transition to well-defined faceted Li polyhedra in all electrolytes (Fig. 1f–i and Supplementary Fig. 3). The trend in polyhedra size in the four electrolytes (spanning from 0.4 to 1.2 µm) corresponds well with the differing electrodeposition overpotential (Supplementary Fig. 4), which is consistent with classical nucleation theory[33]. Additionally, we note that there exists a minimum current density sufficient to outpace SEI influence that will change depending

on cell geometry, temperature, pressure, electrolyte chemistry and other factors. It is not the scope of this initial work to quantify or understand how the minimum current density changes with such parameters (Supplementary Fig. 5) but rather, to demonstrate the implications for surpassing this threshold.

Indeed, these faceted Li polyhedra appear identical across distinct electrolyte chemistries (Fig. 1f–i), which suggests three important findings. (1) The morphology dependence on electrolyte chemistry disappears at ultrafast current densities, (2) Li deposition and SEI formation can be decoupled at ultrafast current densities and (3) the faceted polyhedra are the intrinsic deposition morphology of Li metal in the absence of SEI influence[34]. The well-defined faceted particle shape implies that they are rhombic dodecahedra, which match the thermodynamic Wulff construction of a bcc crystal with only {110} planes exposed as surfaces. For a bcc crystal, the {110} faces are the most densely packed planes, and thus, exposing their lowest-energy surface would minimize the energy of the system. We must note, however, that these scanning electron microscopy (SEM) observations are merely qualitative based on the morphology and crystallographic understanding of Li metal itself. For more quantitative crystallographic evidence of the intrinsic Li deposition morphology being rhombic dodecahedra, we leverage the powerful cryo-EM to preserve the pristine surfaces of the faceted Li polyhedra.

Within the electron microscope, selected area electron diffraction (SAED) can identify the crystalline planes exposed on the Li facets, and high-resolution imaging can reveal the atomic structure of the individual faceted Li particle. First, we deposit Li metal directly onto copper (Cu) transmission electron microscopy (TEM) grids at low current density as a control sample (Supplementary Fig. 6a). Combining cryo-EM imaging and the corresponding SAED pattern (Fig. 2a–c), Li in electrolyte C grows as a single crystalline nanowire along the <211> direction (blue arrow), which is one of the common growth directions of Li dendrites[4]. The lattice spacing of 1.44 Å was obtained in the high-resolution image (Fig. 2c) and matched with the Li {211} plane[4]. Similar results in electrolytes A and D can be found in Supplementary Fig. 7. To grow faceted Li polyhedra at ultrafast current densities on TEM grids (Supplementary Fig. 6b), we modify stainless steel TEM grids with electrodeposited Cu nanowires to serve as local UMEs, producing high electric fields[35] that locally concentrate electrolyte cations during ultrafast deposition. The bcc Li metal crystal has a space group of $Im\bar{3}m$ and a corresponding rhombic dodecahedral geometry as predicted by the Wulff construction (Fig. 2d)[34]. When viewing the two-dimensional projection of a rhombic dodecahedron using cryo-EM, we expect a hexagonal shape (Fig. 2e) when Li is aligned along the <111> zone axis and a square shape (Fig. 2f) when aligned along the <001> zone axis. Indeed, we do observe such shapes: a hexagon in Fig. 2g, where its corresponding SAED pattern (Fig. 2h) confirms its alignment along the <111> zone axis, and a square in Fig. 2j, where its corresponding SAED pattern (Fig. 2k) confirms its alignment along the <001> zone axis. The red arrows in the hexagonal SAED pattern (Fig. 2h) represent the {110} direction pointing toward the reciprocal space reflections (Fig. 2g, circled in red), which correspond to the {110} family of planes. These same arrows overlaid on the hexagonal Li metal polyhedra point toward the edge facets, which directly confirms that these surfaces are {110} planes (Fig. 2g). This same analysis allows us to assign the crystal facets for the surfaces exposed in the square Li projection along the <001> zone axis, all of which are also the {110} planes (Fig. 2j). These cryo-EM data showing the only exposed surfaces being the {110} planes confirm the native Li deposition morphology without SEI influence to be that of a rhombic dodecahedron.

High-resolution cryo-EM images of the faceted Li polyhedra (Fig. 2i,l) resolve individual Li atoms, showing that these deposits are single crystalline and expose the {110} facets. At the atomic scale, the lattice spacings are measured to be 2.48 Å (Fig. 2i,l), which matches well with the known spacing of the Li {110} plane[4]. We note that the surface of Li

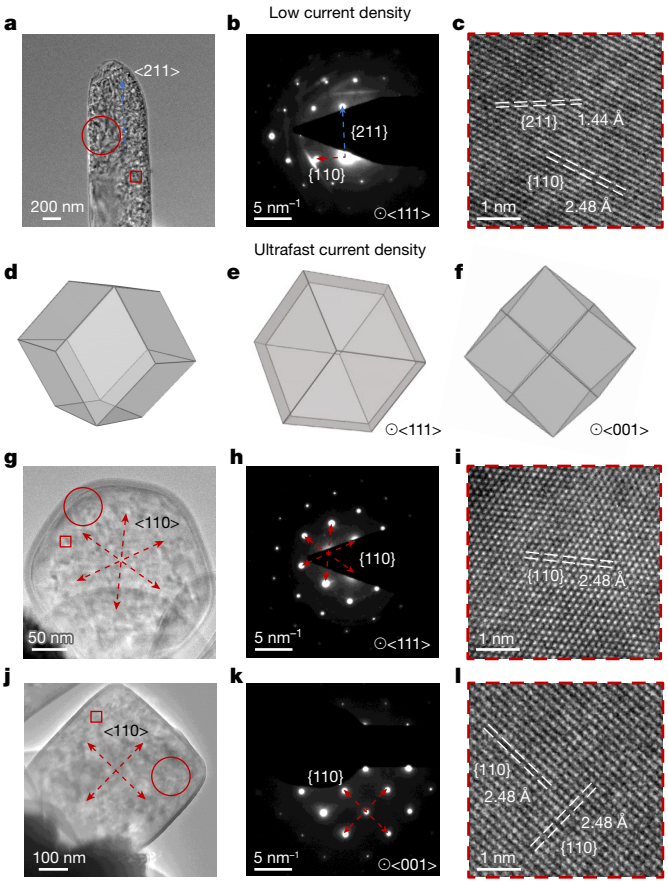

Fig. 2 | Atomic-resolution cryo-EM of Li rhombic dodecahedra with faceting behaviours. a, Cryo-EM image of Li column morphology grown on the Cu TEM grid at low current density. **b**, SAED pattern of the Li column region shown in the red circle of **a**. **c**, High-resolution image of the red boxed region from **a**. **d**, Schematic of bcc Wulff construction. **e**,**f**, bcc Wulff construction shapes aligned along the <111> (**e**) and <001> (**f**) zone axes. **g**, Cryo-EM image of the faceted rhombic dodecahedron Li particle aligned along the <111> zone axis (two-dimensional projection of **e**). **h**, Li metal SAED pattern of the red circled region of **g**. **i**, High-resolution cryo-EM image of the red boxed region from **g**. **j**, Cryo-EM image of the faceted rhombic dodecahedron Li particle aligned along the <001> zone axis (two-dimensional projection of **f**). **k**, Li metal SAED pattern of the red circled region of **j**. **l**, High-resolution cryo-EM image of the red boxed region from **j**. All images correspond to electrolyte C: 0.6 M LiDFOB and 0.6 M $LiBF_4$ in 1:1 v/v FEC/DEC.

polyhedra appears to be covered by an apparent SEI layer, which we propose is the result of inevitable contact between the freshly deposited Li and liquid electrolyte[23,36] after ultrafast deposition during cryo-EM sample preparation that takes on the order of minutes (more than enough time for fresh metallic Li to react chemically with the electrolyte). This is supported by cryo-EM experiments that confirm that Li metal is also deposited as rhombic dodecahedra in electrolytes A and D, demonstrating that the SEI and electrolyte chemistry do not influence the deposition morphology at ultrafast current densities (Supplementary Fig. 8). It is then likely that Li electrodeposition and SEI formation proceed in a stepwise manner when they are decoupled, with Li deposition occurring first electrochemically and SEI formation proceeding chemically after Li deposition. This is supported by cryo-EM and energy-dispersive spectroscopy that confirm structural and chemical differences between SEI formed on faceted Li polyhedra and SEI formed on Li dendrites (Supplementary Fig. 9).

To verify that Li electrodeposition at ultrafast current densities proceeds without SEI influence, we measure Li^+ transport from the bulk to the depositing metallic Li surface in both normal and ultrafast

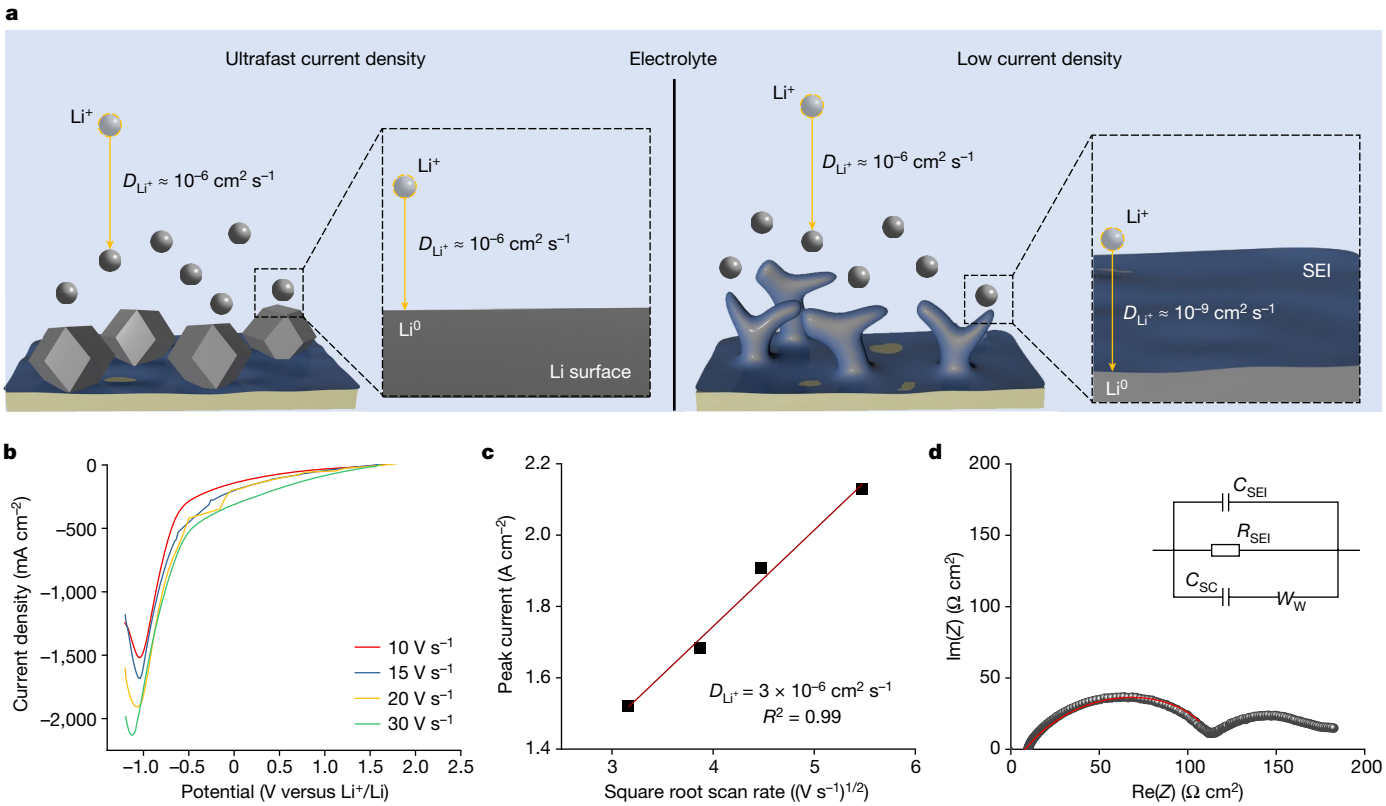

Fig. 3 | Electrochemical analysis of Li plating pathways at ultrafast and low current density regimes. a, Schematic of Li^+ transport from electrolyte to electrode surface without the SEI at ultrafast current density (left) and with the SEI at normal current density (right). **b**, LSV profiles of Li electrodeposition with an ultrafast scan rate from 10 to 30 V s^{-1}. **c**, The dependence of the peak current on the square root of the scan rate. **d**, Nyquist plot of the EIS and the fitting result for the symmetric Li||Li coin cell; the inset is the SEI equivalent circuit model.

current density regimes. Li^+ diffusion coefficients (D_{Li^+}) in the solid (SEI) and liquid (electrolyte) phase are significantly different and often vary by orders of magnitude (Fig. 3a). To measure Li^+ transport at ultrafast current density regimes, linear sweep voltammetry (LSV) experiments with ultrafast scan rates from 10 to 30 V s^{-1} are carried out (Fig. 3b; LSV data with low scan rates are in Supplementary Fig. 10). Figure 3c shows that the peak current density scales linearly with the square root of scan rate, which can be used to calculate a D_{Li^+} value of 3×10^{-6} cm^{-2} s^{-1} (calculation details are in the Methods)[3]. The magnitude of 10^{-6} cm^{-2} s^{-1} is the same as previous measurements[3,37] of D_{Li^+} in liquid electrolytes (Fig. 3a), which indicates that Li^+ transport to the Li–electrolyte interface occurs at the same speed as if in the bulk liquid without SEI interference. To measure Li^+ transport to the Li surface at normal current density regimes, we construct an Li||Li symmetric coin cell to characterize the ionic resistance. This enables calculation of D_{Li^+} from the bulk to the Li surface under normal current density regimes to be 4.4×10^{-9} cm^{-2} s^{-1}. Since Li^+ transport through the SEI accounts for the majority (more than 98%) of the interfacial impedance in an Li||Li cell (Fig. 3d and Supplementary Fig. 11), the dramatic decrease in D_{Li^+} shows that the SEI impedes Li^+ transport under normal current densities[3]. These quantitative measurements show the clear difference in how Li^+ travels from the bulk liquid to the Li surface in the two current density regimes. At ultrafast current densities, Li^+ transport to the surface is on the same order of magnitude as bulk liquid diffusion; at normal current densities, Li^+ transport is slowed by three orders of magnitude and must travel through an SEI layer that is dependent on electrolyte chemistry and controls the Li^+ transport.

While our UME studies are crucial for revealing the intrinsic deposition morphology of Li metal without SEI influence, we further show its implications for operation in coin cell batteries. To confirm that there are no mass transfer limitations at a current density of 50 mA cm^{-2}, we performed COMSOL Multiphysics simulations, showing that the Li^+ concentration gradient can be controlled within 0.3 M from counter to working electrode, and we reach a linear steady state in under 10 s in a coin cell geometry (Supplementary Fig. 12). We successfully deposited Li rhombic dodecahedra at 50 mA cm^{-2} with a capacity of 0.5 mAh cm^{-2} (Fig. 4a and Supplementary Fig. 13a,b; images with 3 mAh cm^{-2} are in Supplementary Fig. 14). In contrast, a column-like Li morphology (Fig. 1b and Supplementary Fig. 13c,d) is observed at 1 mA cm^{-2} with the same capacity and electrolyte chemistry. This finding at ultrahigh current densities subverts conventional wisdom that argues that high current densities are likely to promote more dendritic growth of Li. Instead, we demonstrate that ultrahigh current densities can lead to the non-dendritic growth of Li rhombic dodecahedra as long as mass transport limitations are avoided and the deposition rate can outpace SEI formation. Furthermore, we find that the rhombic dodecahedra structure is independent of the current collector substrate at 50 mA cm^{-2}, regardless of whether the substrate is lithiophobic (for example, Cu, C and so on) or lithiophilic (for example, Au, Ag and so on) (Fig. 4a–d and Supplementary Fig. 15). This finding sharply contrasts with our conventional understanding that the substrate exerts a significant influence on metallic deposition morphology at normal current densities[38]. Since alloy formation kinetics between Au and Li are orders of magnitude slower than the kinetics of SEI formation[39], it stands to reason that if SEI influence is outpaced at ultrafast current densities, the substrate influence is outpaced as well. Although the morphology dependence on substrates disappears at ultrafast current density, the size dependence of Li polyhedra on overpotential remains consistent with nucleation theory[33] (Supplementary Fig. 16). Our results show that it is possible to outpace SEI formation even in a coin cell geometry,

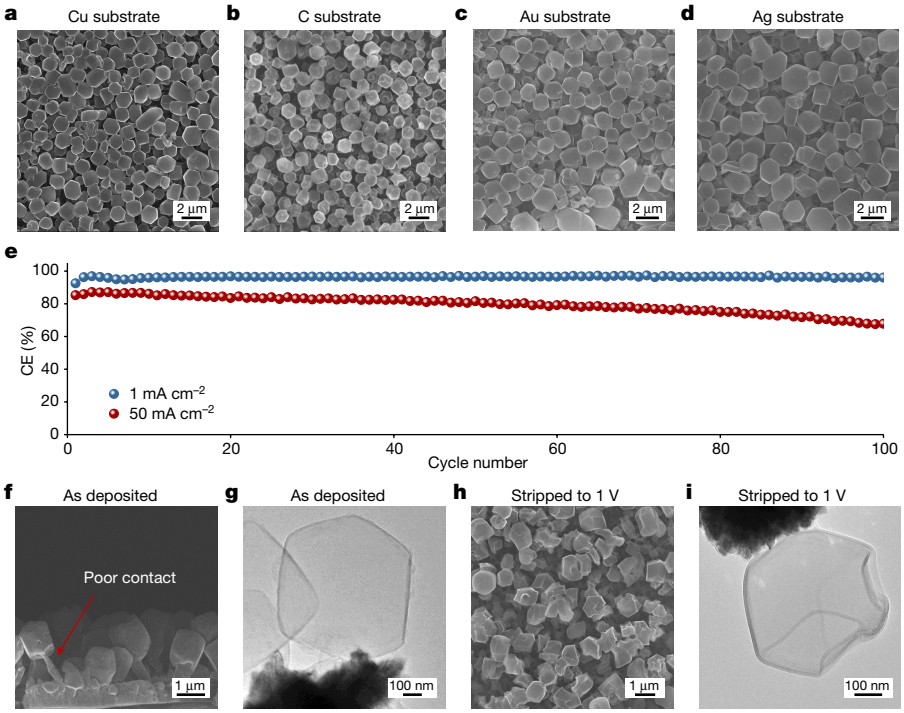

Fig. 4 | Li plating as rhombic dodecahedra in coin cell geometry and its failure mechanism analysis. a–d, SEM images of Li polyhedra grown on Cu (**a**), C (**b**), Au (**c**) and Ag (**d**) substrates at 50 mA cm^{-2}. **e**, CE of Li||Cu cells at current densities of 1 mA cm^{-2} and 50 mA cm^{-2}. **f**,**g**, Cross-sectional SEM view (**f**) and cryo-EM image (**g**) showing poor contact between deposited faceted Li particles and Cu substrate. **h**, Cu foil with abundant inactive Li after stripping with 1 V cutoff voltage. **i**, Cryo-EM image of the partially stripped Li particle after stripping with 1 V cutoff voltage. The electrolyte is C: 0.6 M LiDFOB and 0.6 M $LiBF_4$ in 1:1 v/v FEC/DEC.

allowing us to explore the practical Li plating and stripping behaviours of the unique Li rhombic dodecahedra.

CE quantifies the reversibility of Li deposition and stripping and is a key metric for battery performance. Despite the uniform deposits of Li rhombic dodecahedra, we find that the CE decreases significantly when cycled at 50 mA cm^{-2} compared with CE at 1 mA cm^{-2} (Fig. 4e). Cross-sectional SEM (Fig. 4f) and cryo-EM (Fig. 4g) of the Li rhombic dodecahedra reveal a poor electrical connection with the substrate, which results in dead Li formation during cycling. In contrast, the column-like Li morphologies observed at 1 mA cm^{-2} appear to have more intimate contact with the substrate (Supplementary Fig. 17a). After stripping to 1 V, SEM and cryo-EM imaging show that mostly empty SEI shells remain with limited inactive Li (Supplementary Fig. 17b–d). However, large amounts of remaining Li metal can be observed after stripping at 50 mA cm^{-2} (Fig. 4h). Detailed cryo-EM images show that the rhombic dodecahedron morphology cannot be fully stripped due to poor electrical contact with the substrate, instead exhibiting a partially shrunken structure (Fig. 4i). This indicates that the inactive Li formed through electrical disconnection with the current collector contributes to the decreased CE. Despite this poor initial contact between Li rhombic dodecahedra and the current collector, we can still leverage the well-defined Li {110} surfaces of the Li polyhedra for improved deposition morphology and battery performance. Specifically, we use a pulse-current deposition approach in electrolyte A to first nucleate Li rhombic dodecahedra at ultrafast current densities (50 mA cm^{-2} for 0.05 mAh cm^{-2}) followed by Li growth at normal current densities (1 mA cm^{-2} for 0.95 mAh cm^{-2}) for a total areal capacity of 1 mAh cm^{-2}. SEM images show that Li rhombic dodecahedra are indeed formed after ultrafast deposition (Supplementary Fig. 18a), which serves as a well-defined nucleation surface and facilitates the subsequent growth of dense Li metal during the normal current density deposition (Supplementary Fig. 18c,e). In contrast, constant current deposition at 1 mA cm^{-2} for a capacity of 1 mAh cm^{-2} results in highly dendritic and porous Li morphology in the same electrolyte (Supplementary Fig. 18d,f), leading to potential opportunities for electrical disconnection and inactive Li formation. Nucleation and growth of metallic Li on existing Li {110} surfaces of rhombic dodecahedra will result in denser Li films than Li deposition onto the bare polycrystalline Cu surface[40], resulting in this morphology difference. Furthermore, this difference in deposition morphology between the two charging protocols results in a 5% CE increase (Supplementary Fig. 19a) for the pulse-current protocol. For more advanced electrolytes like electrolyte C, although the baseline performance using constant current is already high, we still observe an approximately 1% CE increase with the pulse-current protocol (Supplementary Fig. 19b). This initial result highlights how our discovery of the intrinsic Li deposition morphology and its origin can be leveraged to provide important and practical implications for advancing battery research.

In conclusion, our work here challenges two long-standing axioms of Li electrodeposition: (1) that high current densities promote dendritic Li growth and (2) that electrolyte chemistry governs Li deposition morphology. During ultrafast electrodeposition that avoids Li^+ depletion, our UME and cryo-EM studies reveal the intrinsic morphology of Li metal to be a non-dendritic rhombic dodecahedron, which is independent of electrolyte chemistry and matches the theoretical Wulff construction of a bcc crystal. Furthermore, we demonstrate how such current density regimes can induce unique failure modes that can be mitigated through a pulse-charging protocol. By outpacing SEI formation and decoupling it from Li metal growth, we open up new opportunities to explore how reactive metal deposition fundamentally proceeds without the influence of a surface corrosion film and its impact on battery operation.

Online content

Any methods, additional references, Nature Portfolio reporting summaries, source data, extended data, supplementary information,

acknowledgements, peer review information; details of author contributions and competing interests; and statements of data and code availability are available at https://doi.org/10.1038/s41586-023-06235-w.

1. Liu, B., Zhang, J.-G. & Xu, W. Advancing lithium metal batteries. *Joule* **2**, 833–845 (2018).
2. Peled, E. The electrochemical behavior of alkali and alkaline earth metals in nonaqueous battery systems—the solid electrolyte interphase model. *J. Electrochem. Soc.* **126**, 2047–2051 (1979).
3. Boyle, D. T. et al. Transient voltammetry with ultramicroelectrodes reveals the electron transfer kinetics of lithium metal anodes. *ACS Energy Lett.* **5**, 701–709 (2020).
4. Li, Y. et al. Atomic structure of sensitive battery materials and interfaces revealed by cryo–electron microscopy. *Science* **358**, 506–510 (2017).
5. Li, Y. et al. Correlating structure and function of battery interphases at atomic resolution using cryoelectron microscopy. *Joule* **2**, 2167–2177 (2018).
6. Li, Y., Li, Y. & Cui, Y. Catalyst: how cryo-EM shapes the development of next-generation batteries. *Chem* **4**, 2250–2252 (2018).
7. Zhang, E. et al. Expanding the cryogenic electron microscopy toolbox to reveal diverse classes of battery solid electrolyte interphase. *iScience* **25**, 105689 (2022).
8. Fang, C. et al. Quantifying inactive lithium in lithium metal batteries. *Nature* **572**, 511–515 (2019).
9. Lin, D., Liu, Y. & Cui, Y. Reviving the lithium metal anode for high-energy batteries. *Nat. Nanotechnol.* **12**, 194–206 (2017).
10. Xu, W. et al. Lithium metal anodes for rechargeable batteries. *Energy Environ. Sci.* **7**, 513–537 (2014).
11. Liu, B. et al. Coupling a sponge metal fibers skeleton with in situ surface engineering to achieve advanced electrodes for flexible lithium-sulfur batteries. *Adv. Mater.* **32**, e2003657 (2020).
12. Peled, E. & Menkin, S. Review—SEI: past, present and future. *J. Electrochem. Soc.* **164**, A1703–A1719 (2017).
13. Bai, P., Li, J., Brushett, F. R. & Bazant, M. Z. Transition of lithium growth mechanisms in liquid electrolytes. *Energy Environ. Sci.* **9**, 3221–3229 (2016).
14. Ren, X. et al. Guided lithium metal deposition and improved lithium Coulombic efficiency through synergistic effects of LiAsF6 and cyclic carbonate additives. *ACS Energy Lett.* **3**, 14–19 (2017).
15. Zhang, Y. et al. Dendrite-free lithium deposition with self-aligned nanorod structure. *Nano Lett.* **14**, 6889–6896 (2014).
16. Qian, J. et al. Dendrite-free Li deposition using trace-amounts of water as an electrolyte additive. *Nano Energy* **15**, 135–144 (2015).
17. Weber, R. et al. Long cycle life and dendrite-free lithium morphology in anode-free lithium pouch cells enabled by a dual-salt liquid electrolyte. *Nat. Energy* **4**, 683–689 (2019).
18. Zhang, W. et al. Colossal granular lithium deposits enabled by the grain-coarsening effect for high-efficiency lithium metal full batteries. *Adv. Mater.* **32**, e2001740 (2020).
19. Qian, J. et al. High rate and stable cycling of lithium metal anode. *Nat. Commun.* **6**, 6362 (2015).
20. Zhou, S. et al. Incorporation of LiF into functionalized polymer fiber networks enabling high capacity and high rate cycling of lithium metal composite anodes. *Chem. Eng. J.* **404**, 126508 (2021).
21. Zheng, J. et al. Regulating electrodeposition morphology of lithium: towards commercially relevant secondary Li metal batteries. *Chem. Soc. Rev.* **49**, 2701–2750 (2020).
22. Xu, K. Nonaqueous liquid electrolytes for lithium-based rechargeable batteries. *Chem. Rev.* **104**, 4303–4418 (2004).
23. Odziemkowski, M. & Irish, D. E. An electrochemical study of the reactivity at the lithium electrolyte/bare lithium metal interface. I. Purified electrolytes. *J. Electrochem. Soc.* **139**, 3063–3074 (1992).
24. Verbrugge, M. W. & Koch, B. J. Microelectrode investigation of ultrahigh-rate lithium deposition and stripping. *J. Electroanal. Chem.* **367**, 123–129 (1994).
25. Boyle, D. T. et al. Resolving current-dependent regimes of electroplating mechanisms for fast charging lithium metal anodes. *Nano Lett.* **22**, 8224–8232 (2022).
26. Boyle, D. T. et al. Correlating kinetics to cyclability reveals thermodynamic origin of lithium anode morphology in liquid electrolytes. *J. Am. Chem. Soc.* **144**, 20717–20725 (2022).
27. Mao, H. et al. Current-density regulating lithium metal directional deposition for long cycle-life Li metal batteries. *Angew. Chem. Int. Ed.* **60**, 19306–19313 (2021).
28. Jiang, F. & Peng, P. Elucidating the performance limitations of lithium-ion batteries due to species and charge transport through five characteristic parameters. *Sci. Rep.* **6**, 32639 (2016).
29. Du, Z., Wood, D. L., Daniel, C., Kalnaus, S. & Li, J. Understanding limiting factors in thick electrode performance as applied to high energy density Li-ion batteries. *J. Appl. Electrochem.* **47**, 405–415 (2017).
30. Jurng, S., Brown, Z. L., Kim, J. & Lucht, B. L. Effect of electrolyte on the nanostructure of the solid electrolyte interphase (SEI) and performance of lithium metal anodes. *Energy Environ. Sci.* **11**, 2600–2608 (2018).
31. Cao, X. et al. Monolithic solid–electrolyte interphases formed in fluorinated orthoformate-based electrolytes minimize Li depletion and pulverization. *Nat. Energy* **4**, 796–805 (2019).
32. Yu, Z. et al. Molecular design for electrolyte solvents enabling energy-dense and long-cycling lithium metal batteries. *Nat. Energy* **5**, 526–533 (2020).
33. Pei, A., Zheng, G., Shi, F., Li, Y. & Cui, Y. Nanoscale nucleation and growth of electrodeposited lithium metal. *Nano Lett.* **17**, 1132–1139 (2017).
34. Sekerka, R. F. Equilibrium and growth shapes of crystals: how do they differ and why should we care? *Cryst. Res. Technol.* **40**, 291–306 (2005).
35. Liu, M. et al. Enhanced electrocatalytic CO_2 reduction via field-induced reagent concentration. *Nature* **537**, 382–386 (2016).
36. He, X. et al. The passivity of lithium electrodes in liquid electrolytes for secondary batteries. *Nat. Rev. Mater.* **6**, 1036–1052 (2021).
37. Gunnarsdóttir, A. B., Vema, S., Menkin, S., Marbella, L. E. & Grey, C. P. Investigating the effect of a fluoroethylene carbonate additive on lithium deposition and the solid electrolyte interphase in lithium metal batteries using in situ NMR spectroscopy. *J. Mater. Chem. A* **8**, 14975–14992 (2020).
38. Yan, K. et al. Selective deposition and stable encapsulation of lithium through heterogeneous seeded growth. *Nat. Energy* **1**, 16010 (2016).
39. Behling, C., Mayrhofer, K. J. J. & Berkes, B. B. Formation of lithiated gold and its use for the preparation of reference electrodes—an EQCM study. *J. Solid State Electrochem.* **25**, 2849–2859 (2021).
40. Hu, X., Gao, Y., Zhang, B., Shi, L. & Li, Q. Superior cycle performance of Li metal electrode with {110} surface texturing. *EcoMat* **4**, e12264 (2022).

Methods

Preparation of electrolyte solutions

LiDFOB (Sigma-Aldrich, ≥99%), $LiBF_4$ (Sigma-Aldrich, ≥98%), $LiAsF_6$ (Sigma-Aldrich, 98%), $LiPF_6$ (Thermo Scientific Chemicals, 98%) and LiFSI (Canrd, 99.5%) were dried at 65 °C overnight before using. FEC (Alfa Aesar, 98%) and DEC (Sigma-Aldrich, 99%) were added to obtain a solution of 0.6 M LiDFOB and 0.6 M $LiBF_4$ (0.6 M LiDFOB and 0.6 M $LiBF_4$ in 1:1 v/v FEC/DEC). Similarly, PC (Alfa Aesar, 99%) and FEC were added to obtain a solution of 1 M $LiPF_6$ in PC with 2 wt% $LiAsF_6$ and 2 wt% FEC. DME (Sigma-Aldrich, 99.5%) was added to obtain a 4 M solution of LiFSI (4 M LiFSI in DME). $LiPF_6$ solution in EC and DEC (1 M $LiPF_6$ in 1:1 v/v EC/DEC) was directly purchased from Sigma-Aldrich with battery grade. All chemicals were used as received without further purification. All electrolytes were made and stored in the Ar-filled glove box (O_2 < 0.2 ppm, H_2O < 0.02 ppm).

Preparation of UME electrodes

A tungsten (W) wire (Goodfellow, 99.95%) of 25 μm in diameter was threaded through the borosilicate glass pipet. The glass pipet tip was carefully melted using a butane torch lighter to achieve a perfect glass-to-metal sealing[41], which should prevent any leakage and bubbles between glass insulation and the W wire. Copper (Cu) wire was electrically connected to sealed W wire using silver paste and served to connect with potentiostat (BioLogic VMP3). The open space of the electrode was filled with insulating epoxy. The prepared UME electrode was polished with a 0.1 micron diamond lapping disc and rinsed with ultrapure water (18.25 MΩ cm^{-1}) and acetone before each experiment. Once dry, UME electrodes were placed in the glove box for usage. The Cu UME electrode was constructed similarly to W UME, except that 25-μm W wire was replaced by Cu wire of 255 μm in diameter.

Electrochemical experiments

The UME-based reactor is a 20-ml beaker cell with 2 ml electrolyte and consists of two electrodes, where the UME electrode served as the working electrode and Li foil (0.75 mm thick, Alfa Aesar, 99.9%) of 10 mm in diameter was used as the counter/reference electrode. Li metal with a capacity of 0.5 mAh cm^{-2} was deposited onto the working electrode by applying a constant current of 10 to 1,000 mA cm^{-2}.

In Li||Cu 2032-type coin cells, Cu foil (10 μm thick, Canrd, 99%) of 4 mm in diameter served as the working electrode, and Li foil of 2 mm in diameter served as the counter/reference electrode to avoid mass transport limitations at high current densities needed to outpace SEI formation. Cu foil was rinsed with ultrapure water and acetone to remove surface contaminants before transferring into the glove box. Li foil was mechanically sheared using a polyethylene scraper to remove the surface oxide and improve electrical connection to the stainless steel coin cell case. Sixty microliters of electrolyte was added to each cell using a 25-μm-thick polypropylene–polyethylene–polypropylene separator (Celgard 2325) to divide the two electrodes. Coin cells were loaded onto a battery tester (Land Instruments) and cycled. For other current collector substrates, Ag and Au foils were prepared by e-beam evaporation with a thickness of 200 nm on Cu foil. Graphite paper was bought from Digi-Key Electronics with a thickness of 70 μm.

The assembly of symmetric Li||Li 2032-type coin cells was the same as Li||Cu cells, except that two polished and flattened 1 cm^2 discs of Li foils served as working and counter electrodes. Electrochemical impedance spectroscopy (EIS) measurements were performed at open circuit after approximately 5 min of assembly with a frequency range of 1 MHz to 0.2 Hz and a perturbation amplitude of 5 mV.

Transient LSV measurements were performed with three-electrode beaker cells with iR-correction. The W UME electrode served as the working electrode, while the Li foil of 10 mm in diameter was used for both the counter and reference electrode. The W UME electrode was swept from open circuit voltage to −1.2 V with different scan rates[3]. At the slow scan rates of 10 and 50 mV s^{-1}, we can see that no obvious peak current density is reached, suggesting that the measurement is a steady-state voltammogram. As the scan rate was increased by three orders of magnitude (10–30 V s^{-1}), the current density–potential response changed. The current density increased sharply after overcoming the nucleation barrier, corresponding to the growth of Li metal, until a current density reached a diffusion-limited peak.

All experiments were performed in the Ar-filled glove box.

Fabrication of Cu chunks-based TEM grids by electrodeposition

Thirty-five milligrams of Cu (II) acetate ($Cu(CO_2CH_3)_2$, Acros, 99%) and 1.3 g sodium citrate tribasic dihydrate ($Na_3C_6H_5O_7{\cdot}2H_2O$, Sigma-Aldrich, ≥99%) were added into 10 ml of ultrapure water to obtain the aqueous electrolyte. The electrodeposition reactor is a 20-ml beaker with 10 ml electrolyte and consists of two electrodes, in which a 100-mesh stainless steel TEM grid (SPI) was used as the working electrode and a graphite rod (Canrd) served as the counter electrode. Cu chunks with a capacity of 0.5 mAh were deposited onto the working electrode by applying a constant current of 10 mA for 3 min. The prepared Cu TEM grid was cleaned with ultrapure water and dried in a vacuum oven until it was placed in the glove box for use.

SEM sample preparation and imaging

After running the electrochemical experiments described above in the glove box, UME electrode, Cu foil or TEM grid working electrode was gently rinsed with a few drops of anhydrous dioxolane and then affixed to an SEM sample stage using conductive tape after drying. The SEM stage with samples was placed in a Teflon box and tightly sealed by parafilm. The pressure in the glove box and thus, the sealed box was greater than ambient pressure, which prevented air from leaking into the box. Once taken out of the glove box, the SEM stage was quickly transferred into the SEM chamber (approximately 5 s) to avoid air exposure. All SEM characterizations were conducted using ZEISS Supra 40VP SEM with a 10-kV acceleration voltage.

Cryo-EM sample preparation and imaging

Coin cells were constructed as usual but with a customized TEM grid incorporated onto the Cu foil as the cocurrent collector. TEM grids with electrodeposited Cu nanostructures were used to serve as local UMEs, producing high electric fields[35] that locally concentrate electrolyte cations to promote ultrafast Li deposition with an estimated current density of 200 mA cm^{-2}, while 300-mesh Cu TEM grids were used for normal Li deposition with an estimated current density of 10 mA^{-2}. To facilitate observation of individual particles under cryo-EM, a capacity of 0.1 mAh cm^{-2} was applied for all cryo-EM samples. After assembling the coin cell in an Ar-filled glove box, the TEM grid was carefully rinsed with a few drops of anhydrous dioxolane. Once dry, the TEM grid with deposited Li was placed in an Eppendorf tube sealed with parafilm and transferred out of the glove box. The pressure in the glove box and thus, the sealed tube was greater than ambient pressure, which prevented air from leaking into the tube. Outside the glove box, pincer pliers held the sealed Eppendorf tube and plunged it quickly into a bath of liquid nitrogen; then, they quickly crushed open the tube after 3 s while still immersed in the liquid nitrogen to expose the grid with deposited Li to cryogen immediately. The grid was stored in a cryo-grid box in liquid nitrogen dewar for usage.

To proceed with cryo-EM imaging, the TEM grid was mounted onto a Gatan 626 TEM cryo-transfer holder using a cryo-transfer station to make sure the whole process took place under liquid nitrogen. The built-in shutter on the transfer holder was kept closed to prevent air exposure and ice condensation on the sample when inserting the holder into the TEM column (approximately 1 s). A liquid nitrogen dewar attached to the holder maintained the grid at cryogenic

temperature (approximately −178 °C) during the whole imaging process. All cryo-EM characterizations were carried out using an FEI Titan 80–300 scanning transmission electron microscope operated at 300 kV. The microscope was equipped with a field-emission gun, an energy-dispersive X-ray spectroscopy detector and an ultrascan 2 × 2 K digital camera. During cryo-EM images acquisition, the corresponding electron dose flux was also recorded. Electron dose rate is less than 100 e $Å^{-2}$ s^{-1} for low magnification cryo-EM images and less than approximately 1,000 e $Å^{-2}$ s^{-1} for high-resolution cryo-EM images. The electron beam exposure time of each image is no more than 30 s, and the acquisition time is 0.4 to 1 s.

EIS fitting

The Nyquist plot (Fig. 3d) displays two distinct semicircles. One semicircle comprises the high- to midfrequency range (that is, more than 20 Hz) that is typically attributed to Li^+ transport through the compact SEI layer. The second semicircle corresponds to the low-frequency range (that is, less than 20 Hz) that is attributed to transport through the extended SEI, which comprises electrolyte degradation products not directly interfacing with the metallic Li[7]. The extended SEI is not a rate-determining step for Li^+ transfer. Therefore, the fitting process was performed for the high- to midfrequency range (the first semicircle) corresponding to the compact SEI layer directly interfaced with the Li metal. This is a reasonable approximation and has been used in previous studies[25,42] quantifying Li^+ transport through the SEI film. Although there are a number of equivalent circuit models[43,44] for SEI that give similar results, we chose a particular model (Fig. 3d) that is relatively simple for the charge transfer process of the SEI on empirical analysis[45,46]. In addition, this equivalent circuit has recently been leveraged for its simplicity and accuracy in extracting physical parameters and predicting properties of a model SEI system[42]. A schematic of the SEI model corresponding to the equivalent circuit is shown in Supplementary Fig. 11, and the fitting process was completed using the ZFit unit in EC-Lab software. The equivalent circuit consists of a resistor (R_{SEI}) representing the resistance of Li^+ transport through the SEI, a capacitor (C_{SC}) representing the space charge capacitance, a capacitor (C_{SEI}) representing the dielectric response of the SEI and a Warburg diffusion element (W) representing Li^+ diffusion through the SEI. The interfacial charge transfer kinetics (that is, $Li^+ + e^- \rightarrow Li^0$) was neglected in this equivalent circuit since previous study suggested that this is a reasonable approximation[3]. Based on the above circuit model and fitting the result of EIS, we calculate an SEI ionic resistance of $R_{SEI} = 115\ \Omega$.

Ionic transport parameters calculation through the SEI

The conductivity of the SEI (λ_{SEI}) is calculated by

$$\lambda_{SEI} = \frac{l_{SEI}}{R_{SEI}A} = 1.4 \times 10^{-8}\ (\Omega\,\mathrm{cm})^{-1},$$

where l_{SEI} is the SEI thickness measured by statistics from cryo-EM images (Supplementary Fig. 9d) and A is the electrode area. Traditionally, the Nernst–Einstein equation establishes a relationship between ionic conductivity and ion diffusion coefficients. Thus, experimental measurements of SEI conductivity can be used to calculate ion diffusion coefficients according to the Nernst–Einstein equation, which has been widely adopted by the battery community[42].

The diffusion coefficient of Li^+ through SEI ($D_{Li^+}^{SEI}$) is calculated by

$$D_{Li^+}^{SEI} = (\lambda_{SEI} Z_W A)^2 = 4.4 \times 10^{-9}\ \mathrm{cm^2\ s^{-1}},$$

where Z_W is the Warburg element, and it was obtained from the EIS equivalent circuit fitting.

The carrier concentration (n) of Li^+ in the SEI is calculated by the Nernst–Einstein equation,

$$n = \frac{\lambda_{SEI} RT}{F^2 D_{Li^+}^{SEI}} = 8.4 \times 10^{-7}\ \mathrm{mol\ cm^{-3}},$$

where T is the temperature, R is the standard gas constant and F is the Faraday constant.

The above calculated results are consistent with previous studies of Li^+ transport in the SEI[37,42].

Diffusion coefficient of Li^+ through electrolyte D_{Li^+} calculation

For a total irreversible one-step, one-electron reaction ($Li^+ + e^- \rightarrow Li$), the Nernst equation and boundary condition can be used to calculate the relationship between peak current density J_p and the effective diffusion coefficient D_{Li^+}:

$$J_p = (2.99 \times 10^5)\alpha^{1/2} C_{Li^+}^{*} D_{Li^+}^{1/2} v^{1/2},$$

where α is the transfer coefficient and $C_{Li^+}^{*}$ is the bulk concentration of Li^+.

The transfer coefficient describes how strong the rate of an electrochemical reaction depends on the applied potential. In most electrochemical systems, the transfer coefficient is assumed to be constant and typically lies between 0.3 and 0.7. It is approximated as 0.5 in the absence of actual measurements:

$$D_{Li^+} = 3 \times 10^{-6}\ \mathrm{cm^2\ s^{-1}}.$$

COMSOL Multiphysics simulations

The simulations are performed on COMSOL Multiphysics v.5.6 using the physics module of 'Electrochemistry-Battery' and Butler–Volmer expressions of hydrodynamics. Due to three-dimensional cell geometry being symmetrical along the height of the battery, a two-dimensional cross-section is used to model the three-dimensional geometry of the battery. The electrochemical model consists of an electrolyte domain and two electrode boundaries. Since the electronic conductivity of Cu and Li metal is very high and the electrochemical deposition reactions only take place at the surface of the Cu electrode, the thickness of metal is neglected in the model geometry. In UME geometry, the module of electric field distribution is 500 × 2,000 μm^3 with the standard electrolyte of 1 M $LiPF_6$ in 1:1 v/v EC/DEC running at a current density of 1,000 mA cm^{-2} at 298 K. Parameters (for example, ionic conductivity, viscosity and so on) of the electrolyte for simulation are given in Supplementary Table 1. The designed working electrode is 25 μm in diameter, and other parts are set to be insulated. In coin cell geometry, the module of electric field distribution is 50 × 2,000-μm^3 filling with the same electrolyte running at a current density of 50 mA cm^{-2} at 298 K. The time-dependent simulation is applied, and an initialization study step is used to calculate the initial potentials in the cell; 1.8-s (UME geometry) and 36-s (coin cell geometry) time-dependent solvers are set up to store the solution at 0.1-s intervals.

Data availability

The data that support the findings of this study are available from the corresponding author on reasonable request.

41. Sur, U. K., Dhason, A. & Lakshminarayanan, V. A simple and low-cost ultramicroelectrode fabrication and characterization method for undergraduate students. *J. Chem. Educ.* **89**, 168–172 (2011).
42. Guo, R. & Gallant, B. M. Li_2O solid electrolyte interphase: probing transport properties at the chemical potential of lithium. *Chem. Mater.* **32**, 5525–5533 (2020).
43. Peled, E., Golodnitsky, D. & Ardel, G. Advanced model for solid electrolyte interphase electrodes in liquid and polymer electrolytes. *J. Electrochem. Soc.* **144**, L208 (1997).
44. Verbrugge, M. W. & Koch, B. J. Microelectrode study of the lithium/propylene carbonate interface: temperature and concentration dependence of physicochemical parameters. *J. Electrochem. Soc.* **141**, 3053–3059 (1994).

45. Churikov, A. V., Gamayunova, I. M. & Shirokov, A. V. Ionic processes in solid-electrolyte passivating films on lithium. *J. Solid State Electrochem.* **4**, 216–224 (2000).
46. Churikov, A. V., Nimon, E. S. & Lvov, A. L. Impedance of Li-Sn, Li-Cd and Li-Sn-Cd alloys in propylene carbonate solution. *Electrochim. Acta* **42**, 179–189 (1997).

Acknowledgements We acknowledge the support of the National Science Foundation (CBET-2143677) and the use of the University of California, Los Angeles California NanoSystems Institute EICN Facilities.

Author contributions X.Y. and Y.L. conceived the project and designed the experiments. X.Y. built the UME set-up and performed electrochemical experiments and SEM characterization. B.L. helped with COMSOL simulations and data analysis. X.Y. and Y.L. carried out cryo-EM experiments. M.M. advised on microscope and imaging analyses. X.Y. and Y.L. co-wrote the manuscript. All authors discussed the results and commented on the manuscript.

Competing interests The authors declare no competing interests.

Additional information
Supplementary information The online version contains supplementary material available at https://doi.org/10.1038/s41586-023-06235-w.
Correspondence and requests for materials should be addressed to Yuzhang Li.
Peer review information *Nature* thanks Shizhao Xiong and the other, anonymous, reviewer(s) for their contribution to the peer review of this work.